Hybrid Propulsion In-Situ Resource Utilization Test Facility Results for Performance Characterization

F. S. Mechentel*

Stanford University, Stanford, CA, 94305, USA

A. C. Karp †, B. Nakazono ‡, M. Parker §, and D. Vaughan ¶

Jet Propulsion Laboratory, California Institute of Technology, Pasadena, CA, 91109, USA

Hybrid propulsion presents a promising alternative to conventional systems for in-space propulsion applications using In-Situ Propellant Production (ISPP). A hybrid propulsion test facility has been built at the NASA Jet Propulsion Laboratory (JPL) with the capability of evaluating ISPP oxidizers (gaseous mixtures of O_2 and CO_2) and modifying fuel type and chamber geometry. This work is the result of a continuing effort at JPL to characterize the burn characteristics and performance of different propellant combinations and motor configurations in order to refine and support preliminary designs. Twelve tests using gaseous oxygen and two paraffin based fuels (Black Paraffin and SP1X) from the 2015 campaign are presented. Different reduction techniques are compared in an effort to determine the uncertainty associated with deriving a regression rate law and evaluating c* efficiency with the collected data.

Nomenclature

L	Length, m or in	*Subscript*	
D	Diameter, m or in		
P	Pressure, bar or psi	c	combustion chamber
t_b	Burn time, s	$fuel$	fuel grain
G	Mass flux, g/cm^2/s	$orifice$	oxidizer sonic orifice
$\dot{m}$	Mass flow, g/s	inj	injector
O/F	Oxidizer to fuel ratio	nt	nozzle throat
m	Mass, kg	ox	oxidizer
ρ	Density, kg/m^3	p	port
A	Area, m^2	i	initial
C_v	Venturi velocity coefficient	f	final
Z	Compressibility factor	out	outer
C_d	Nozzle discharge coefficient	1	venturi inlet
E	Random relative error	2	venturi throat

I. Introduction

Hybrid motors are mechanically and chemically simple propulsion systems that have the potential for long-term storability with low gross mass. The oxidizer (such as gaseous O_2) can be produced in-situ, significantly reducing the landed mass. The solid, inert fuel is stored in the combustion chamber in its most

*PhD Candidate, Department of Aeronautics and Astronautics, Stanford University, AIAA Member

†Propulsion Engineer, JPL Propulsion and Fluid Flight Systems, M/S 125-211, AIAA Member.

‡Senior Propulsion Engineer, JPL Propulsion and Fluid Flight Systems, M/S 125-211, AIAA Member.

§Senior Propulsion Engineer, JPL Propulsion and Fluid Flight Systems, M/S 125-211, AIAA Member.

¶Group Supervisor, JPL Propulsion and Fluid Flight Systems, M/S 125-211, AIAA Member.

dense state, further reducing the total structural mass and volume. Considerable efforts have been focused on ISPP for Environmental Control and Life Support Systems (ECLSS) and human exploration of Mars. At optimum oxidizer to fuel ratio (O/F), about 70% of the total propellant mass could be produced in-situ. Paraffin based fuels exhibit a fast regression rate behavior due to the formation of a thin liquid layer on the fuel surface.[1] A high burn rate is necessary in order to reach a medium to high thrust range. In order to achieve an O/F ratio close to optimum performance (between 2.1 and 2.7 for the O_2/Paraffin combination), the fuel mass flow needs to be sufficiently large compared to the oxidizer flow. The slow regression rate of classical hybrid rocket fuels leads to long fuel grain designs or complicated multi-port structures. Single port, high regression rate fuels have the potential to reduce residual propellant mass and have a grain length to diameter ratio (L/D) more favorable for packaging. However, hybrid motors remain at a fairly low Technology Readiness Level (TRL), and solutions to accurately measure and increase performance are still lacking, especially for small-scale motors that are constrained to tight packaging.

A total of 12 hotfires were performed and analyzed in this campaign. All of these tests were conducted at pressures above the critical pressure of paraffin wax, approximately 6.7 bar (97 psi).[2] Three different motor configurations were explored while conserving a single cylindrical port fuel grain. Additionally, since throttling is a crucial advantage of hybrid rocket propulsion systems, low oxidizer mass flows (60 - 100 g/s) and fluxes (5 - 30 g/cm^2/s) were investigated to determine the performance impact in this regime.

II. Test Facility

A. Existing Set Up Overview

A hybrid propulsion test facility was developed in 2014 to answer some of the open questions in the field. The system design and capabilities are discussed in ref.,[3] and the main constraints are restated below.

- Maximum thrust: 222 N (50 lbf)
- Fuel grain outer diameter: 5.1 cm (2.0 in)
- Maximum expected operating chamber pressure: 17.2 bar (250 psi)
- Maximum oxidizer upstream pressure: 68.9 bar (1000 psi)

The instrumentation capabilities of the test facility in 2014 are shown in figure 1 and measure the following using LabView control:

- Oxidizer upstream pressure P1 (1 kHz)
- Oxidizer mass flow using a custom venturi, differential pressure transducer (1 kHz), pressure P2 (1 kHz), temperature T2 (K-type, 10 Hz)
- Chamber pressure P3A (1 kHz) for all tests and P3B (1 kHz) for tests after #12

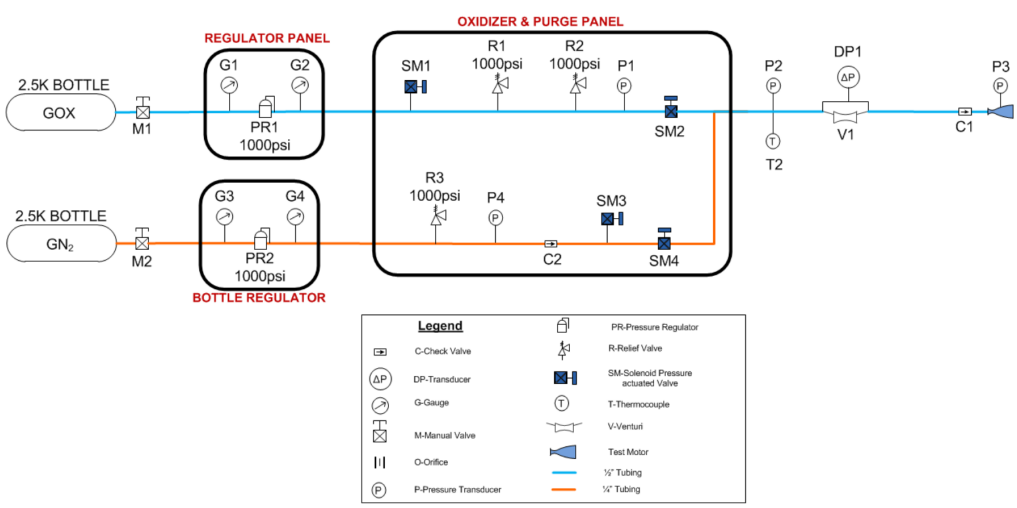

Figure 1. Piping and instrumentation diagram of the test facility in 2014.

Modifications that were made before and during the 2015 campaign are discussed in the next section. This flexible design allows several motor variations listed below.

- Oxidizer: gaseous O_2 or gaseous mixtures of O_2 and CO_2
- Fuel: variable initial diameter and length
- Chamber length: 10.2 cm (4.0 in), 20.3 cm (8.0 in) or 30.5 cm (12.0 in)
- Nozzle: throat diameter of 1.22 cm (0.48 in) or 1.52 cm (0.60 in)

Two motor configurations were tested and are shown in figure 2. The nominal design has a converging diverging nozzle right after the fuel grain. The second configuration uses a graphite post-combustion chamber.

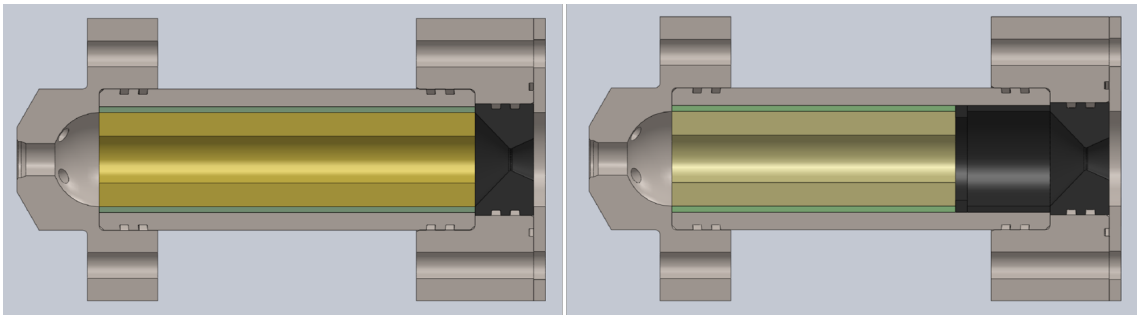

Figure 2. Motor configurations. Left: without post-combustion chamber. Right: with 5.1 cm (2 in) post-combustion chamber.

The tests reported here were run with pure Gox and high melt temperature paraffin wax from the Candlewic company (160°F Melt Point - 5560 paraffin wax) mixed with back dye (0.5 % by mass), or a black paraffin based fuel containing strength additives (SP1X) procured from the Space Propulsion Group, Inc. (SPG). Note that the dye is added in hope to prevent the radiative heat transfer from penetrating deep into the fuel grain. Candlewic paraffin material properties such as volatiles released, phase transition and coefficient of thermal expansion were obtained and described in ref.[4] The fuel grains were centrifugally cast in a Flame-Retardant Garolite (G10/FR4) thermal insulator using a dedicated casting system at JPL. It is possible to test alternative fuel types since the only constraints are length and outer diameter.

A custom ignition system[4] using a small amount of a pyrotechnic mixture is used to pyrolize some of the paraffin and initiate combustion with the oxidizer. Proper manufacturing of these igniters is crucial for short hotfires (around 3 s) since it affects the start-up transient duration. The initiators work in two stages and most failures are due to the loose initiation powder not igniting the slower burning secondary charge.

All firings are conducted at ambient external pressure and temperature (typically between 15 and 30°C in Southern California) and are recorded for each test along with the humidity level. A proportional, integral, derivative-based feedback control system maintains a constant pressure upstream of the sonic orifice. Thrust is not measured and the nozzle expansion ratio (different for the small (AR=3.52) and large (AR=2.25) nozzles) does not affect any of the acquired data.

B. Modifications for the 2015 Campaign

Minor modifications were made before and during the test campaign. Two sonic orifices (⌀=0.925 in and ⌀=0.14 in) were used. This component is located about 9.5 cm (3.75 in) upstream of the injector. The smaller orifice coupled with a differential pressure transducer (max ΔP = 30 psi) can control and measure mass flow rates from 30 to 60 g/s. The larger orifice coupled with a ΔP transducer (max 100 psi) can achieve flow rates between 50 and 110 g/s. Two 9-hole injectors (one center hole and eight surrounding) were manufactured to ensure that the oxidizer enters the combustion chamber at a Mach number around 0.2 for each orifice. A second pressure transducer was added at the fore end of the motor as can be seen in figure 3.

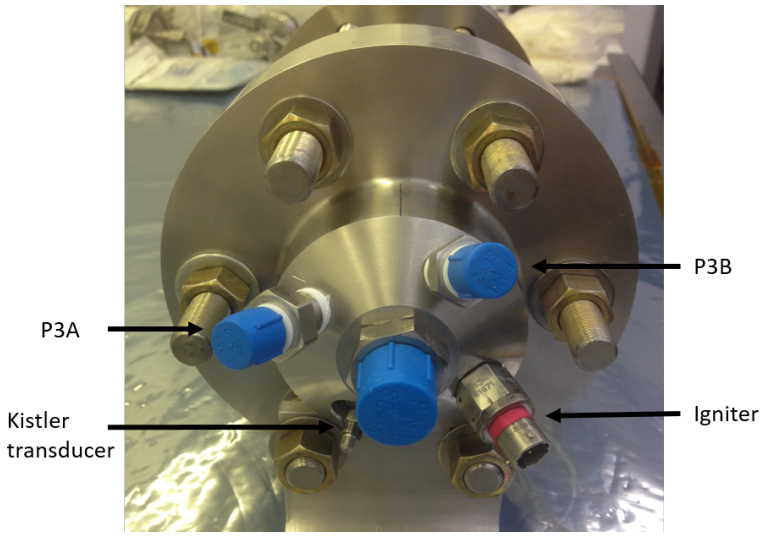

Figure 3. Hybrid motor fore end cap.

III. Hotfire Results and Discussion

A total of 12 hotfires varying different parameters (table 1) were performed. A still image of a motor hotfire test is shown in figure 4. The test numbering starts at #10 for consistency with the previous campaign.[4] BP refers to Black Paraffin procured from the Candlewic company and SP1X to SPG's paraffin based formulation. The maximum burn time was set to reach the longest steady state duration without fully consuming the fuel to collect regression rate measurements. Reduction techniques for spatially and temporally averaging data are discussed below.

Table 1. Summary of test parameters.

Test #	Fuel	L_c [cm]	L_{fuel} [cm]	$D_{orifice}$ [mm]	D_{inj} [mm]	D_{nt} [cm]
10	BP	10.2	10.2	2.35	1.32	1.2
11	BP	10.2	10.2	2.35	1.32	1.2
12	BP	20.3	20.3	3.57	1.99	1.5
13	BP	20.3	20.3	3.57	1.99	1.5
14	BP	20.3	15.2	3.57	1.99	1.5
15	SP1X	20.3	15.2	3.57	1.99	1.5
16	SP1X	20.3	15.2	3.57	1.99	1.5
17	SP1X	20.3	15.2	3.57	1.99	1.5
18	SP1X	20.3	15.2	3.57	1.99	1.5
19	SP1X	20.3	15.2	3.57	1.99	1.2
20	SP1X	20.3	15.2	3.57	1.99	1.5
21	SP1X	20.3	15.2	3.57	1.99	1.5

Figure 4. Still image taken from the video of hotfire test #18, O_2/SP1X, P_c= 7.10 bar (103 psi).

A. Burn Time and Chamber Pressure

Determining the test start and end times is of utmost importance to calculate temporally averaged values. A typical pressure-time curve for these tests has a short start-up transient corresponding to the time required to initiate the reaction and reach a stable operating pressure and a longer shut-down transient. After the main oxidizer flow valve is closed, the chamber pressure smoothly decreases to ambient pressure before the nitrogen purge gas is introduced in the chamber. The duration of these transient events is not consistent between tests and can depend on the ignition procedure or the LabView control sequence. For this series of hotfires the pyrotechnic igniters were not identical and small differences in charge mass, packaging, and secondary charge thru-hole diameter can drastically change the start-up behavior of the motor. To compare various data reduction methods and evaluate sources of uncertainty related to burn time and temporally averaged values, six different schemes are used:

- M : (Manual) determine the start and end points to only conserve stable operating regime
- 90% : Start and end at 90% of the average chamber pressure found using [M]
- 50% : Start and end at 50% of the average chamber pressure found using [M]
- ASM : (Ambient Start/Manual) Start when P_c is 10% higher than ambient pressure and use the end point from [M]
- MAE : (Manual/Ambient End) Start point from [M] and end when P_c reaches 10% of P_{amb}
- A : (Ambient) Start when P_c is higher than 10% of P_{amb} and end when P_c is lower than 10% of P_{amb}

Table 2. Summary of burn times, mean values and standard deviations in seconds, obtained using different reduction techniques.

Test #	t_{b_M}	$t_{b_{90\%}}$	$t_{b_{50\%}}$	$t_{b_{ASM}}$	$t_{b_{MAE}}$	t_{b_A}	Mean	Std dev	Notes
10	3.15	3.19	3.32	3.40	3.62	3.88	3.43	0.25	
11	3.00	3.18	3.36	4.35	3.52	4.87	3.71	0.67	delayed ignition
12	3.10	3.27	3.34	3.27	3.45	3.63	3.34	0.16	
13	3.15	3.21	3.27	3.30	3.46	3.61	3.33	0.15	
14	3.15	3.28	3.36	3.30	3.46	3.61	3.36	0.15	
15	2.60	2.83	2.90	2.84	2.95	3.19	2.89	0.18	
16	3.30	3.56	3.64	3.54	3.63	3.87	3.59	0.17	
17	2.60	3.03	3.26	3.15	2.96	3.51	3.09	0.28	long start-up, G10 aft plate
18	3.40	3.64	3.73	3.59	3.69	3.88	3.66	0.15	
19	1.80	1.94	2.08	3.81	2.10	4.11	2.64	0.94	erratic start-up
20	2.60	2.82	2.90	2.79	2.91	3.10	2.85	0.15	
21	3.45	3.72	3.80	3.68	3.79	4.01	3.74	0.17	

The chamber pressure transducer was changed during the campaign and a second transducer was added for tests #12 and above for measurement redundancy. Although these two transducers consistently tracked pressure variations quite well, a small offset was reported for each test and is given in table 3. Additionally, the measurements began to diverge after repeated use (for subsequent tests not reported here). The average of the two measurements was used when both transducers were installed. It was observed that the fore end of the motor was covered in a thin layer of paraffin wax after each hotfire. Although the pressure ports were never plugged, the transducers had a large amount of solid wax in the cavity that was delicately removed to not affect later test measurements. A small amount of Krytox grease was added before each test to protect the diaphragm from the hot gases. It is to be noted that a thin G10 plate was added between the grain and post-combustion chamber for test #17 to reduce the high burn rate at the aft end of the fuel. This test is not considered in the data analysis discussed in further sections.

Table 3. Summary of chamber pressures in bar (psi) obtained using different reduction techniques.

Test #	P_{c_M}	$P_{c_{90\%}}$	$P_{c_{50\%}}$	$P_{c_{ASM}}$	$P_{c_{MAE}}$	P_{c_A}	$\lvert P_{3A} - P_{3B} \rvert$
10	10.0 (145)	10.0 (145)	9.9 (143)	9.5 (137)	9.3 (135)	8.9 (129)	NA
11	9.6 (139)	9.6 (139)	9.5 (137)	7.6 (110)	9.0 (130)	7.3 (106)	NA
12	11.6 (168)	11.6 (168)	11.5 (167)	11.2 (162)	11.1 (161)	10.8 (157)	$\approx$ 2 (30)
13	12.3 (179)	12.5 (181)	12.4 (180)	11.9 (172)	11.9 (173)	11.5 (167)	$\approx$ 1.3 (19)
14	11.0 (160)	11.0 (160)	11.0 (159)	10.7 (155)	10.6 (154)	10.3 (150)	$\approx$ 1 (15)
15	9.0 (131)	9.0 (131)	9.0 (130)	8.6 (125)	8.6 (125)	8.3 (120)	$\approx$ 0.5 (7)
16	8.3 (120)	8.3 (120)	8.3 (120)	8.1 (117)	8.00 (116)	7.9 (114)	$\approx$ 0.4 (6)
17	8.8 (128)	8.8 (127)	8.6 (125)	8.4 (122)	8.5 (123)	8.1 (118)	$\approx$ 0.8 (12)
18	7.1 (103)	7.1 (103)	7.0 (102)	7.0 (101)	7.0 (101)	6.8 (99)	$\approx$ 0.5 (7)
19	9.2 (133)	9.2 (133)	9.0 (130)	5.9 (85)	8.7 (126)	5.9 (85)	$\approx$ 0.5 (7)
20	8.2 (119)	8.1 (118)	8.1 (117)	8.0 (116)	7.9 (114)	7.7 (112)	$\approx$ 0.6 (9)
21	8.3 (120)	8.2 (119)	8.1 (118)	8.1 (117)	7.9 (115)	7.8 (113)	$\approx$ 0.2 (3)

Manually selecting start and end points in the pressure trace for the averaging process is very subjective. Therefore, the [M] method can be considered less reliable and a large amount of error in the burn time estimation can be introduced. However, selecting this interval is useful in order to compute the average chamber pressure during steady state operation. Taking a percentage of this value (50 or 90%) proved to be a consistent method that depended very little on the exact selection of the averaging bounds. The [ASM] method is the most difficult to implement since the start up behavior of the motor is not always consistent. Additionally, the measured pressure before ignition is not reliable because it is at the lower end of the operating range of the pressure transducer (less than 10% or 50 psi), which is known to have reduced accuracy. Using a low pressure measurement (used with the [ASM], [MAE] and [A] methods) is therefore not recommended and explains the wide spread of burn time measurements in table 2.

A large offset was observed between the two pressure transducers for tests #12, 13 and 14. This offset was reduced by changing the P3A instrument with one identical to P3B (max 500 psi). The difference between these two measurements is an indicator of the uncertainty related to chamber pressure measurements since they should be identical. Although the locations of the pressure ports are close (figure 3), the distance and angle compared to the igniter port could have a large influence on the measurement. Figure 5 shows chamber pressures for several different tests and illustrates the difficulties associated with determining burn time and average chamber pressure.

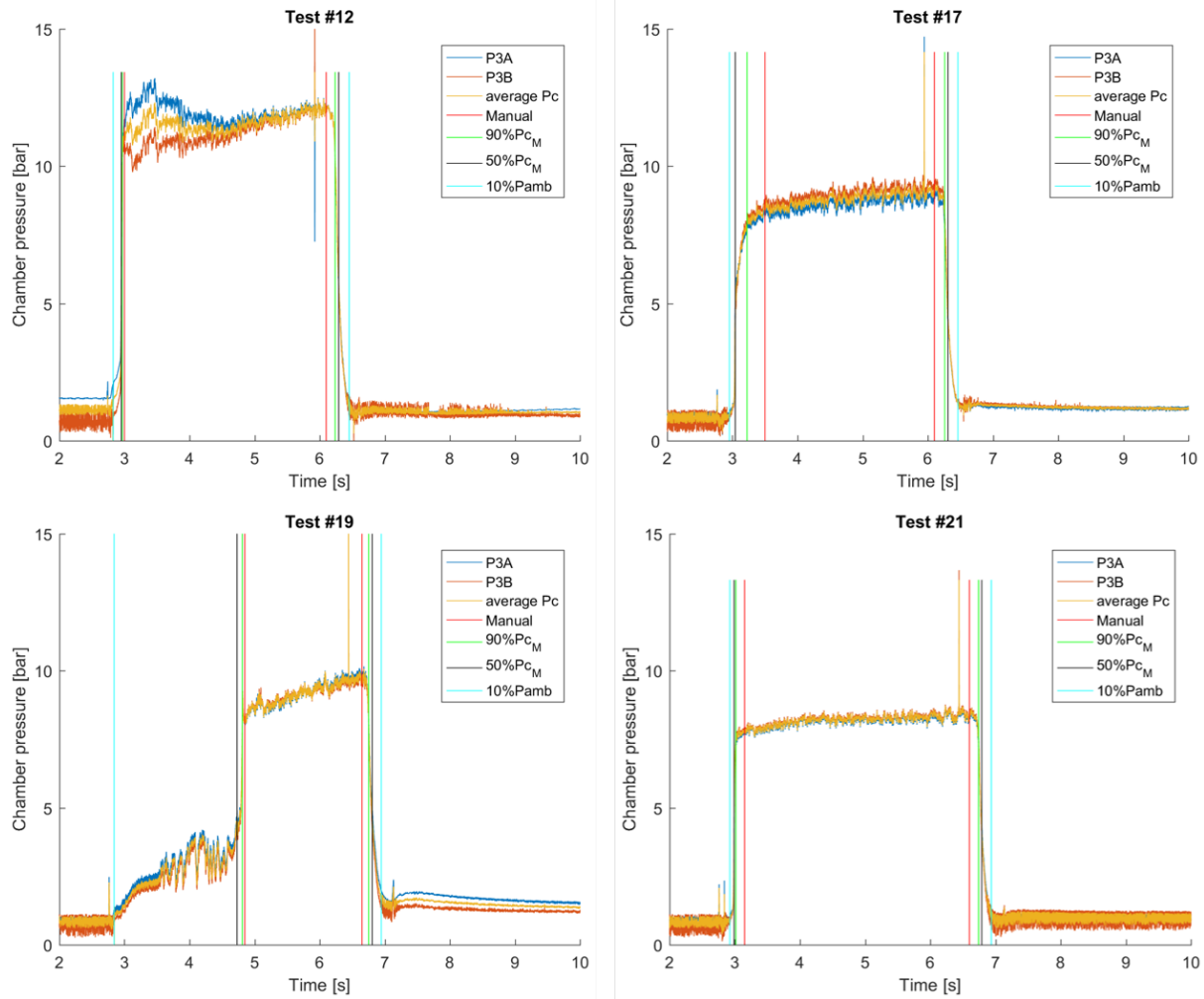

Figure 5. Time pressure variations for different tests. Top left: large offset between P3A and P3B ($\approx$ 2 bar). Top right: long start-up transient ($\approx$ 2 s). Bottom left: erratic ignition behavior. Bottom right: stable operation.

It was observed that the chamber pressure increases during the burn for all tests and this phenomenon is still not well understood. The regulated oxidizer pressure does not increase during the test resulting in a quasi constant oxidizer mass flow. Therefore, the increase in pressure can only be due to an increase in fuel mass flow (inconsistent with a flux dependent cylindrical regression rate model) or a decrease in nozzle throat area due to thermal effects. The large pressure spike observed in all pressure traces in figure 5 near shutdown is due to an electrical interference.

B. Oxidizer Mass Flux

Space and time averaging is required to determine the oxidizer mass flux used to derive a regression rate law for a given propellant combination. For these calculations, the fuel grain is assumed to burn uniformly along the length of the grain and conserve a cylindrical geometry. Karabeyoglu et. al.[5] studied three reduction methods including diameter, area and flux averaging. The port diameter averaging method is shown to have the smallest error and is used here (Eq. 1).

$$\bar{G}_{ox} \cong \frac{16\bar{\dot{m}}_{ox}}{\pi(D_{p,i} + D_{p,f})^2} \tag{1}$$

However, there are different ways to measure or estimate the initial and final inner port diameters of the fuel grain. The first is to measure the thickness of the fuel grain at different angular locations at the fore

and aft ends before and after each firing. This procedure was carried out for each test and clearly shows the axial variation of the regression rate since the aft end thicknesses are always smaller than the fore end measurements, meaning that the regression rate of the fuel is higher at the aft end than at the fore end. It is to be noted that measuring the thickness between the outside of the thermal insulator and the inner port is more favorable than trying to measure the inner port diameter directly using calipers. The measurements using the previously described method are shown in figure 6 for a BP grain (test #14) and an SP1X grain (test #15). Four equally spaced measurements are taken pre firing (red) and 8 post firing (blue) and an average diameter is computed. This figure alone shows that BP regresses faster than SP1X and that SP1X conserves a more cylindrical geometry since the measured points are closer to the mean diameter (dashed line).

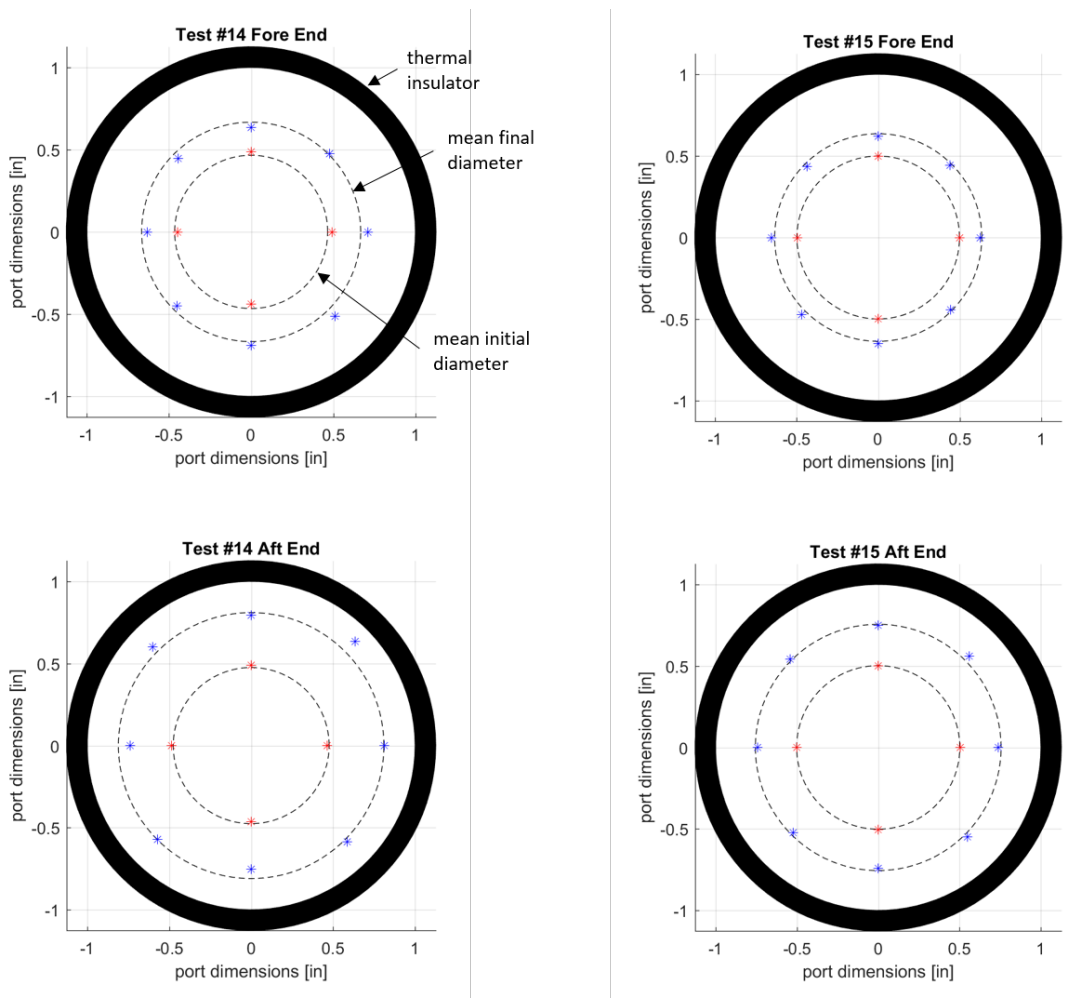

Figure 6. Initial and final, fore and aft end port dimensions for tests BP #14 (left) and SP1X #15 (right).

Although this method seems straightforward, a large error can be introduced since the initial port diameter is not always uniform. The centrifugal casting process creates a fair amount of coning near the end caps and leads to a larger thickness measurement and ultimately overestimates the initial oxidizer mass flux and fuel regression rate. For better consistency, all SP1X cast fuel grains were eventually post machined and the inner diameter was bored out evenly to the desired initial diameter.

A second method using the initial and final masses of the fuel grain was considered.[5] Using the fuel density and outer fuel grain diameter, the initial and final space averaged diameters are solved using Eq. 2, assuming a cylindrical geometry. However, during this campaign the densities of the fuel grains were not properly established and this introduces significant error. Paraffin wax and SPG fuels have been known to have densities around 930 kg/m^3. The crudest method to determine the density of a cylindrical fuel grain is to use the mass, and inner and outer diameters. Each fuel grain mass was recorded with the G10 insulation mass. Error is introduced when subtracting the insulator mass which is not measured separately but estimated using a linear density. The outer diameter of the fuel grain corresponds to the inner diameter of the G10 insulation ($D_{out} \approx 5.1$ cm (2.0 in)) and was not measured prior to spin casting. Manufacturing tolerances are not given by the supplier. As a result, insufficient data was collected to apply this method reliably. Testing procedures would need to be corrected for future data processing to include weighing the initial fuel mass without the casting cartridge, and measuring the density for each fuel grain.

$$\begin{cases} D_{p,i} \cong \sqrt{{D_{out}}^2 - \dfrac{4m_{fuel,i}}{\pi \rho_{fuel} L_{fuel}}} \\ D_{p,f} \cong \sqrt{{D_{out}}^2 - \dfrac{4(m_{fuel,i} - m_{fuel,f})}{\pi \rho_{fuel} L_{fuel}}} \end{cases} \tag{2}$$

As previously mentioned, oxidizer mass flow is calculated with a calibrated venturi coupled with a differential pressure transducer (Eq. 3). Cold flow measurements were compared to mass loss in the cylinder (ref.[4]). Using a velocity coefficient C_v of 1, the measured and calculated values were within 5-10% of each other. The compressibility coefficient is calculated using the Van der Waals equation and was found to be around 0.95.

$$\bar{\dot{m}}_{ox} = C_v Z A_2 \sqrt{\frac{2\rho_{ox}\bar{\Delta P}}{1 - \left(\frac{A_2}{A_1}\right)^2}} \tag{3}$$

Analyzing the differential pressure transducer data is not trivial since large and rapid pressure variations are not well captured by the instrument and the quasi-steady state assumption used to derive Eq. 3 no longer holds. The same behavior was consistently seen for all cold flows and hotfires and is shown in figure 7. When the main valve is opened, the ΔP sensor data is beyond the maximum measurement capability and when the main valve is shut a large negative signal is observed. As a result, it is difficult to identify the portion of the data representative of the reality. Consequently, the constant stable portion of the data is manually identified and averaged. This mean oxidizer mass flow $\bar{\dot{m}}_{ox}$ is used for all further calculations. This is a reasonable assumption based on the stability of the pressure traces shown in figure 7. A summary of the processed data is shown in table 4.

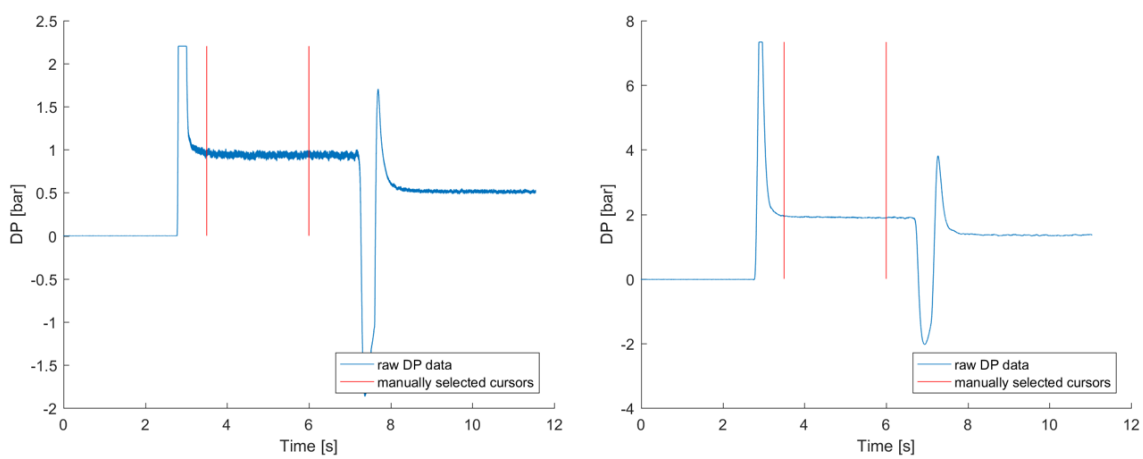

Figure 7. Differential pressure across the venturi for Test #11, 30 dpsi transducer (left) and test #19, 100 dpsi transducer (right).

Table 4. Summary of fuel initial and final diameters, oxidizer mass flows, and fluxes.

Test #	$D_{p,i}$ [cm (in)]	$D_{p,f}$ [cm (in)]	$\bar{\dot{m}}_{ox}$ [g/s]	$\bar{G}_{ox}$ [kg/m^2/s]
10	2.45 (0.97)	3.90 (1.54)	57	73
11	2.37 (0.93)	3.74 (1.47)	51	70
12	2.13 (0.84)	3.85 (1.52)	95	135
13	2.13 (0.84)	3.87 (1.52)	105	149
14	2.39 (0.94)	3.75 (1.48)	93	126
15	2.54 (1.00)	3.53 (1.39)	79	109
16	2.55 (1.00)	3.79 (1.49)	70	89
17	2.56 (1.01)	3.66 (1.44)	69	91
18	2.52 (0.99)	3.71 (1.46)	59	78
19	2.51 (0.99)	3.17 (1.25)	49	77
20	2.52 (0.99)	3.53 (1.39)	69	95
21	2.52 (0.99)	3.76 (1.48)	69	89

C. Fuel Regression Rate

The classic hybrid regression rate formula, derived by Marxman,[7] assumes that the combustion process is diffusion limited. Using a fully turbulent boundary layer and neglecting radiative effects, the local instantaneous fuel regression rate can be expressed as a function of total mass flux (G), port length coordinate (x), and three empirical coefficients (a, n and m) (Eq. 4). The main characteristic of hybrid rocket combustion is the pressure independence of the recession velocity. However, under very low mass flux conditions the convective heat transfer is low, radiative effects can no longer be neglected, and pressure dependence could be observed. According to Marxman, this regime can lead to poor combustion and unreliable operation. However, a lower mass flux bound has not been clearly identified and the exploration of this potentially damaging regime is necessary for further development of small-scale motors for in-space applications. Although the oxidizer mass flux levels in the present study can be considered low, the regression rate is assumed to not be affected by chamber pressure. Using two different nozzle throat sizes, chamber pressures were kept between 6.9 bar (100 psi) and 12.4 bar (180 psi).

$$\begin{cases} \dot{r} = a_0 G^n x^m \\ G = \dfrac{\dot{m}_{ox} + \dot{m}_{fuel}}{A_{port}} \end{cases} \tag{4}$$

The total propellant mass flux is very difficult to measure experimentally. As a result, this flux is commonly replaced by the oxidizer mass flux (Eq. 5) and corrective terms can be included in the a coefficient. For consistency with the space averaging methods described to calculate oxidizer mass flux, the axial variation is assumed negligible and $m = 0$. The regression rate is in m/s and oxidizer mass flux is kg/m^2/s.

$$\dot{r} = a G_{ox}^n \tag{5}$$

The space time averaged regression rate can be determined using Eq. 6. Proper estimation of the burn time is crucial and will be discussed further. The initial and final port diameters are estimated by averaging the measured fore and aft end diameters (figure 6).

$$\bar{\dot{r}} \cong \frac{D_{p,f} - D_{p,i}}{2t_b} \tag{6}$$

To determine the a and n coefficients given a set of data, a linear fit (in a least squares sense) is found in logarithmic form (Eq. 7). For consistency with similar studies, n=0.62 is used from ref.,[6] where 23 Gox/Paraffin based fuel (SP1-a) tests were analyzed with average oxidizer mass fluxes ranging from approximately 70 to 370 kg/m^2/s. It is to be noted that the burn time used by Karabeyoglu et. al. is the time lapse between the ignition and the valve closing. These events were not recorded by the LabView

system at the time of this study and burn time was exclusively determined from chamber pressure traces. Additionally, the final port diameter was not corrected using the method described in ref.[6]

$$ln(\dot{r}) = n \times ln(G_{ox}) + ln(a) \tag{7}$$

In this analysis, tests #11, 17, and 19 were not considered due to the non standard start-up behavior. The a coefficient was determined separately for BP and SP1X using the 6 reduction methods and results are given in table 5.

Table 5. Summary of a coefficients determined using different reduction techniques with $\dot{r}$ in m/s and $\bar{G}_{ox}$ in kg/m^2/s.

Fuel	a_M	a_{90}	a_{50}	a_{ASM}	a_{MAE}	a_A	Mean	Std dev
BP	1.30e-4	1.26e-4	1.23e-4	1.23e-4	1.17e-4	1.11e-4	1.22e-4	6.23e-6
SP1X	1.13e-4	1.04e-4	1.02e-4	1.05e-4	1.02e-4	9.57e-5	1.04e-4	5.08e-6

Coefficients found in this analysis are in reasonable agreement with the regression rate law proposed by Karabeyoglu et. al. (Eq. 8). However, a large uncertainty is associated with port diameter measurements and many more tests are required to properly quantify the fit of the model.

$$\bar{\dot{r}} = 1.17 \times 10^{-4} \bar{G}_{ox}^{0.62} \tag{8}$$

IV. c* Efficiency

The characteristic velocity (c*) is a commonly used parameter to determine the efficiency of the combustion process independently of thrust and nozzle characteristics. Effects that are known to reduce c* efficiency include incomplete reaction of the propellants and heat losses. Experimentally, c* is calculated with the chamber pressure, total mass flow rate and nozzle throat area. The nozzle discharge coefficient C_d is taken to be 1. Eq. 9 is used here to determine the overall average c* value for a given test.

$$\bar{c^*} = \frac{\bar{P}_c C_d A_{nt}}{\bar{\dot{m}}_{ox} + \frac{m_{fuel}}{t_b}} \tag{9}$$

This experimental setup does not allow us to determine the instantaneous nozzle throat area which may vary due to thermal effects or erosion. The nozzle throat diameter was measured before each motor assembly and did not vary during the campaign. For consistency, all c* calculations reported in the present work were obtained with time averaged values. The ideal c* is computed using the NASA Glenn Thermochemical code CEA (Chemical Equilibrium with Applications)[8] using shifting equilibrium, or equivalently frozen equilibrium at the throat (and not the combustor). Figure 8 shows the results for ideal c* calculations versus O/F ratio using gaseous O_2 and neat Paraffin ($C_{32}H_{66}$, $h_f = -224.193$ kcal/mol). Reactants are at ambient temperature and chamber pressures is varied from 6.9 bar (100 psi) to 13.8 bar (200 psi). These fuel characteristics were used in CEA for both fuel types. At the lower pressure, maximum $c^* = 1,795$ m/s is reached for $O/F = 2.12$. For $P_c = 13.8$ bar, maximum $c^* = 1,807$ m/s is reached for $O/F = 2.16$.

The CEA calculation is carried out using the average chamber pressure obtained with each method from table 3, and respective overall O/F ratio. O/F (table 6) is calculated using the average oxidizer mass flow, burned fuel mass, and the appropriate burn time from table 2. The nozzle throat area is assumed constant. The short burn time suggests that erosion should be minimal and any thermal effects of the graphite nozzle are not taken into account. Thermal expansion would reduce the throat area and increase the c* efficiency.

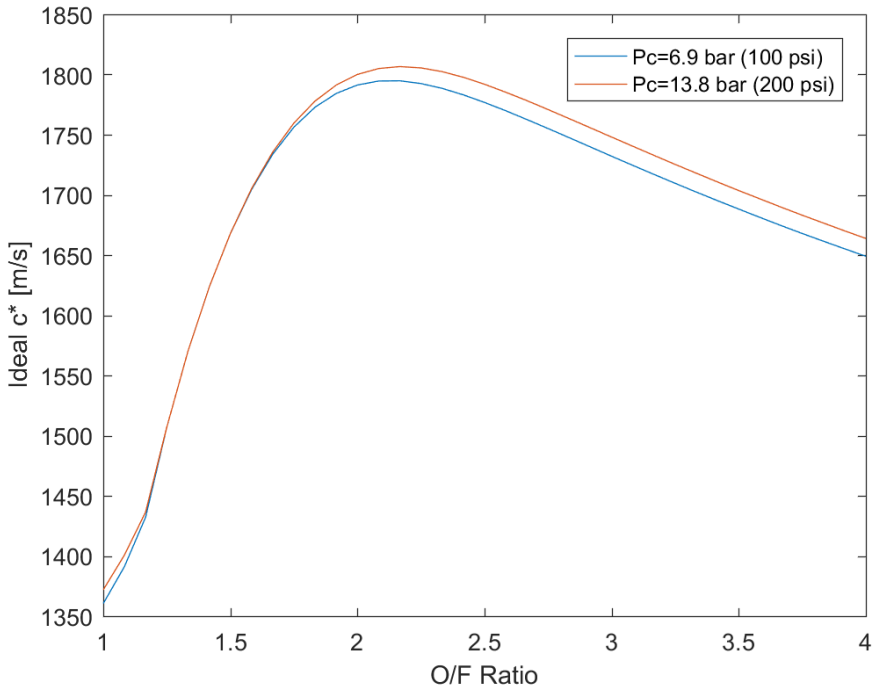

Figure 8. O_2/Paraffin ideal c* computed with CEA for different chamber pressures.

c* calculations using the 6 previously described reduction techniques are given in table 7 (all results are in %). The final values are within about 2-4% of each other for 10 tests out of 12. The larger spreads are observed for tests #11 (delayed ignition), and #19 (erratic start-up behavior). However, using the a priori less reliable methods [ASM], [MAE] and [A] always lead to a more conservative evaluation of the c* efficiency.

Table 6. Summary of O/F ratio using different reduction techniques.

Test #	OF_M	OF_{90}	OF_{50}	OF_{ASM}	OF_{MAE}	OF_A	Mean	Std dev
10	2.29	2.32	2.42	2.48	2.64	2.82	2.49	0.18
11	2.11	2.23	2.36	3.05	2.47	3.42	2.61	0.47
12	1.73	1.82	1.86	1.83	1.93	2.02	1.87	0.09
13	1.85	1.89	1.93	1.94	2.03	2.12	1.96	0.09
14	2.69	2.81	2.87	2.82	2.96	3.09	2.87	0.12
15	2.53	2.76	2.83	2.77	2.88	3.11	2.81	0.17
16	2.32	2.51	2.56	2.49	2.56	2.73	2.53	0.12
17	2.00	2.33	2.51	2.42	2.28	2.70	2.37	0.21
18	2.14	2.29	2.35	2.26	2.32	2.44	2.30	0.09
19	1.80	1.94	2.08	3.81	2.10	4.11	2.64	0.94
20	2.24	2.43	2.50	2.40	2.50	2.66	2.45	0.13
21	2.32	2.50	2.55	2.47	2.54	2.70	2.51	0.11

Table 7. Summary of c* efficiency using different reduction techniques.

Test #	$\eta_{c^*_M}$	$\eta_{c^*_{90}}$	$\eta_{c^*_{50}}$	$\eta_{c^*_{ASM}}$	$\eta_{c^*_{MAE}}$	$\eta_{c^*_A}$	Mean	Std dev
10	78.7	79.0	79.2	76.7	77.4	76.0	77.8	1.2
11	82.4	83.8	84.0	74.6	81.7	75.8	80.4	3.8
12	80.5	81.1	80.9	78.4	78.7	77.3	79.5	1.4
13	78.4	79.4	79.3	76.0	77.1	75.3	77.6	1.6
14	88.7	90.2	90.5	88.0	88.8	88.2	89.0	0.9
15	84.0	86.8	87.1	83.1	84.7	84.0	84.9	1.5
16	83.6	86.1	86.3	83.7	84.2	84.4	84.7	1.1
17	86.3	90.2	91.2	88.0	86.2	89.0	88.5	1.9
18	83.1	85.0	85.2	83.4	83.6	84.1	84.1	0.8
19	79.4	80.6	79.8	66.4	77.8	68.2	75.4	5.8
20	83.4	85.8	86.1	83.7	83.6	84.2	84.5	1.1
21	84.3	86.6	86.8	84.8	84.5	85.2	85.4	1.0

V. Limitations and Uncertainty

A. Non Uniform Regression

The main assumption used for all the calculations in the previous section is the uniform regression of the fuel grain, meaning that it always conserves a cylindrical geometry. Fig. 6 has already shown that significant outward coning was observed for these tests, specifically with the Black Paraffin grains from Candlewic. Additionally, neat paraffin is difficult to centrifugally cast as the thermal stresses during the process can form cracks that propagate axially and radially. Fuel grains with cracks were burned with the objective to determine how detrimental this phenomenon could be if it were to occur after long term storage for example. It was assumed that the liquid layer forming on the fuel surface during combustion could seal the crack and inhibit its growth. However, the fuel consistently regressed faster around the cracks (Fig. 9) and in certain cases even exposed the insulator. This was the main incentive to switch to a fuel formulation such as SP1X that has more reliable structural properties and can be centrifugally cast more easily.

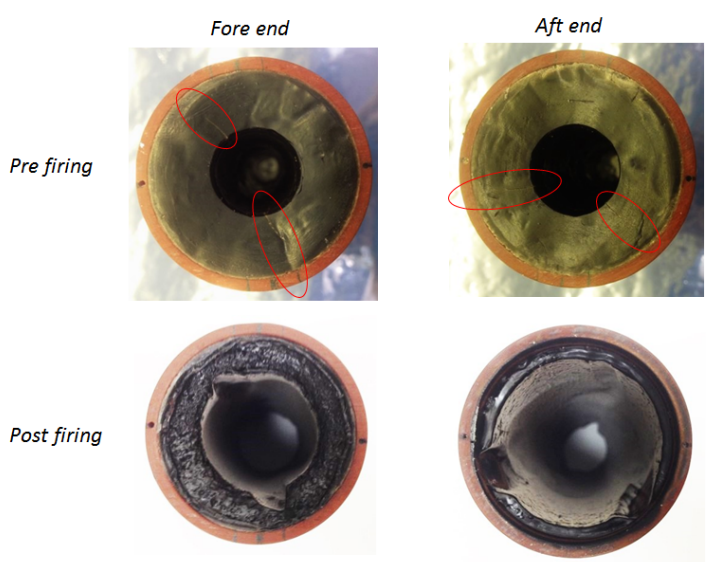

Figure 9. Burning along the cracks created during the casting process for Black Paraffin from the Candlewic company.

A four lobe pattern was consistently observed on all SP1X burned fuel grains (figure 10), making the inner port non cylindrical. It is more pronounced at the aft end of the grain. This geometry is most likely induced either by the injector's hexagonal shape or the four fore end ports (igniter and three pressure taps) shown in figure 3.

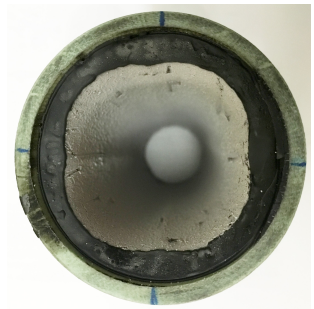

Figure 10. Four lobe pattern observed on all SP1X burned fuel grains.

B. Error Analysis

It is essential to quantify the error associated with determining the regression rate, oxidizer mass flow, oxidizer mass flux, O/F ratio and c* to evaluate the quality of the data. The random error associated with the measurements is derived following the methodology in ref.[5] In Eq. 10, $R = \frac{D_{p,f}}{D_{p,i}}$. The relative error associated with nozzle discharge coefficient, venturi velocity coefficient, oxidizer density, and compressibility factor are neglected.

$$\begin{cases} E_{\dot{r}} = \left[\left(\frac{R}{R-1}E_{D_{p,f}}\right)^2 + \left(\frac{1}{R-1}E_{D_{p,i}}\right)^2 + E_{t_b}^2\right]^{\frac{1}{2}} \\ E_{\dot{m}_{ox}} = \left[\frac{1}{4}E_{\Delta P} + 8E_{D_2} + 4E_{D_1}\right]^{\frac{1}{2}} \\ E_{G_{ox}} = \left[\left(\frac{2R}{R+1}E_{D_{p,f}}\right)^2 + \left(\frac{2}{R+1}E_{D_{p,i}}\right)^2 + E_{\dot{m}_{ox}}^2\right]^{\frac{1}{2}} \\ E_{O/F} = \left[E_{\dot{m}_{ox}}^2 + E_{t_b}^2 + E_{\Delta m_f}^2\right]^{\frac{1}{2}} \\ E_{c^*} = \left[E_{P_c}^2 + 4E_{D_{nt}}^2 + \left(\frac{O/F}{1+O/F}\right)^2 E_{\dot{m}_{ox}}^2 + \left(\frac{1}{1+O/F}\right)^2 E_{t_b}^2 + \left(\frac{1}{1+O/F}\right)^2 E_{\Delta m_f}^2\right]^{\frac{1}{2}} \end{cases} \tag{10}$$

Determining the correct uncertainty for the results presented in this paper is a difficult process. In most cases, the instrumental uncertainty is irrelevant compared to the random uncertainty associated with the user in the case of calipers, data acquisition for pressure measurements, and most importantly data reduction techniques and averaging processes. As a result, crude upper bounds are determined for the relative random error.

The relative error associated to $D_{p,f}$ is assumed to be 0.06 from the measured data, and $E_{D_{p,i}}$=0.03. This error is smaller since the initial fuel thickness is larger and more uniform. The relative error in burn time is determined from the reduction analysis in section III A. The spread from the mean burn time of the 6 different methods is used to determine E_{t_b}. On average, this value was as high as 0.09 excluding tests #11, 17, and 19. For $R = 1.5$, these numbers result in a relative error in regression rate of 21%.

The differential pressure across the venturi ΔP shows little variation and $E_{\Delta P}$ was found to be 0.02 on average. $E_{D_2} = 0.0017$ and $E_{D_1} = 0.0043$. $E_{\dot{m}_{ox}} \approx 1.4\%$.

Using $E_{D_{p,f}}$, $E_{D_{p,i}}$ and $E_{\dot{m}_{ox}}$ previously determined yields $E_{G_{ox}} \approx 7.7\%$ for $R = 1.5$.

The readability of the scale used to measure the mass of the fuel grain before and after the test was ±1 g. On average, the burned fuel mass was 100 g. Using $E_{\Delta m_f} = 0.01$, $E_{O/F} \approx 9.2\%$.

The random uncertainty for c* depends on the O/F ratio. On average, the O/F ratio for these tests was around 2.2. From table 3, $E_{P_c} = 0.042$ was determined. $E_{D_{nt}} = 0.02$. Finally, $E_{c^*} \approx 6.5\%$. The mean relative error calculated using the values in table 7 for the c* efficiency is 2.2%. This suggests that E_{c^*} should not be confused with $E_{\eta_{c^*}}$. In reality, when the burn time is overestimated using method [A] for example, the mean chamber pressure is also reduced, and the total mass flow is increased. These two effects tend to reduce the spread in c* efficiency. Additionally, a higher burn time implies a higher O/F ratio, which, when associated with a lower mean P_c, leads to a lower estimation of the ideal c* value using CEA.

VI. Conclusion

The JPL hybrid propulsion test facility has successfully tested laboratory-scale gaseous oxygen/paraffin based fuel motors. Results from 12 hotfires were analyzed and critically compared. Five tests using black paraffin showed that axial cracks formed during the spin casting process can be accentuated during the burn, rendering the fuel port non cylindrical and possibly exposing the thermal insulation to the hot combustion products. Seven tests using a paraffin based fuel and additives to improve the structural properties of the grain (SP1X) showed no signs of cracking. Six different data reduction techniques were used in an effort to quantify the uncertainty associated with the obtained quantitative data. The random relative error of the burn time is significant (up to 21%) and highly affects the regression rate data and O/F ratio determination (up to 9.2% random relative error). These results show that accurately characterizing the regression rate using short burns is very difficult. However, the spread in c* efficiency using the 6 different reduction methods was relatively small ($\approx \pm 2\%$) when the start-up and shut-down transients were short and consistent.

Many more tests are required to accurately determine the regression rate and c* efficiency of gaseous oxygen and high regression rate fuels to be included in preliminary designs of these motors for future missions. This study is a milestone in testing hybrid rocket motors at JPL, improving testing procedures, and refining data analysis techniques.

Acknowledgments

The research was carried out at the Jet Propulsion Laboratory, California Institute of Technology, under a contract with the National Aeronautics and Space Administration. The authors would like to thank the Jet Propulsion Laboratory for funding this research through its internal Research and Technology Development program. The authors would also like to thank the test team: Lawrence Harma, Matthew Devost, Alex Wolpe, Richard Webster, Alex Luna and William Gavid.

References

[1]M. A. Karabeyoglu, D. Altman, B. J. Cantwell, *Combustion of Liquefying Hybrid Propellants: Part 1, General Theory*, Journal of Propulsion and Power, Vol. 18, No. 3, May-June 2002.

[2]A. Karabeyoglu, B. Cantwell, J. Stevens, *Evaluation of the Homologous Series of Normal Alkanes as Hybrid Rocket Fuels*, 41st AIAA/ASME/SAE/ASEE Joint Propulsion Conference & Exhibit, AIAA 2005-3908.

[3]A. A. Chandler, C. Gatto, B. Nakazono, K. Grayson, D. Vaughan, *Hybrid Propulsion In-Situ Resource Utilization Test Facility Development*, 50th AIAA/ASME/SAE/ASEE Joint Propulsion Conference, AIAA 2014-3866.

[4]A. C. Karp, B. Nakazono, D. Vaughan, W. N. Warner, *Hybrid Propulsion In-Situ Resource Utilization Test Facility Results*, 51st AIAA/ASME/SAE/ASEE Joint Propulsion Conference, AIAA 2015-4200.

[5]M. A. Karabeyoglu, B. J. Cantwell, G. Zilliac, *Development of Scalable Space-Time Averaged Regression Rate Expressions for Hybrid Rockets*, 41st AIAA/ASME/SAE/ASEE Joint Propulsion Conference, AIAA 2005-3544.

[6]A. Karabeyoglu, G. Zilliac, B. Cantwell, S. De Zilwa, P. Castelluci, *Scale-Up Tests of High Regression Rate Paraffin-Based Hybrid Rocket Fuels*, Journal of Propulsion and Power, Vol 20., No. 6, NovDec, 2004.

[7]G. A. Marxman, C. E. Wooldridge, R. J. Muzzy, *Fundamentals of Hybrid Boundary Layer Combustion*, Progress in Aeronautics and Astronautics, Vol. 15, 1964, pp. 485522.

[8]S. Gordon, B. J. McBride, *Computer Program for Calculation of Complex Chemical Equilibrium Compositions and Applications*, NASA Reference Publication 1311, October 1994.

[9]G. Zilliac, A. Karabeyoglu, *Hybrid Rocket Fuel Regression Rate Data and Modeling*, 42nd AIAA/ASME/SAE/ASEE Joint Propulsion Conference, AIAA 2006-4504.

[10]R. A. Frederick Jr., B. E. Greiner, *Laboratory-Scale Hybrid Rocket Motor Uncertainty Analysis*, Journal of Propulsion and Power, Vol. 12, No. 3, May-June 1996.

[11]K. Lohner, J. Dyer, E. Doran, Z. Dunn *Fuel Regression Rate Characterization Using a Laboratory Scale Nitrous Oxide Hybrid Propulsion System*, 42nd AIAA/ASME/SAE/ASEE Joint Propulsion Conference, AIAA 2006-4671.